# Fundamental physics with ESPRESSO: a new determination of the D/H ratio towards PKS1937-101

Francesco Guarneri,[1,2,3]★ Luca Pasquini[1], Valentina D'Odorico[2,4,7], Stefano Cristiani[2,4,5], Guido Cupani[2,4], Paolo Di Marcantonio[2], J. I. González Hernández[9,10], C. J. A. P. Martins[11,15], Alejandro Suárez Mascareño[9,10], Dinko Milaković[4,2,5], Paolo Molaro[2], Michael T. Murphy[8,4], Nelson J. Nunes[14], Enric Palle[9,10], Francesco Pepe[6], Rafael Rebolo[9,10], Nuno C. Santos [15,16], Ricardo Génova Santos[9,10], Tobias M. Schmidt[6], Sérgio G. Sousa[15], Alessandro Sozzetti[12], Andrea Trost[2,3]

[1] *ESO–European Southern Observatory, Karl-Schwarzschild-Strasse 2, 85748 Garching bei München, Germany*
[2] *INAF–Osservatorio Astronomico di Trieste, Via G.B. Tiepolo, 11, I-34143 Trieste, Italy*
[3] *Dipartimento di Fisica, Sezione di Astronomia, Università di Trieste, via G.B. Tiepolo 11, I-34131, Trieste, Italy*
[4] *IFPU–Institute for Fundamental Physics of the Universe, via Beirut 2, I-34151 Trieste, Italy*
[5] *INFN–National Institute for Nuclear Physics, via Valerio 2, I-34127 Trieste, Italy*
[6] *Département d'astronomie, Université de Genève, Chemin Pegasi 51, CH-1290 Versoix, Switzerland*
[7] *Scuola Normale Superiore, P.zza dei Cavalieri, I-56126 Pisa, Italy*
[8] *Centre for Astrophysics and Supercomputing, Swinburne University of Technology, Hawthorn, Victoria 3122, Australia*
[9] *Instituto de Astrofísica de Canarias, E-38205 La Laguna, Tenerife, Spain*
[10] *Universidad de La Laguna, Dept. Astrofísica, E-38206 La Laguna, Tenerife, Spain*
[11] *Centro de Astrofísica da Universidade do Porto, Rua das Estrelas, 4150-762 Porto, Portugal*
[12] *INAF – Osservatorio Astrofisico di Torino, via Osservatorio 20, 10025 Pino Torinese, Italy*
[13] *Instituto de Astrofísica e Ciências do Espaço, Faculdade de Ciências da Universidade de Lisboa, Campo Grande, 1749-016 Lisboa, Portugal*
[14] *Instituto de Astrofísica e Ciências do Espaço, Faculdade de Ciências da Universidade de Lisboa, Campo Grande, PT1749-016 Lisboa, Portugal*
[15] *Instituto de Astrofísica e Ciências do Espaço, CAUP, Universidade do Porto, Rua das Estrelas, 4150-762 Porto, Portugal*
[16] *Departamento de Física e Astronomia, Faculdade de Ciências, Universidade do Porto, Rua Campo Alegre, 4169-007 Porto, Portugal*

Accepted XXX. Received YYY; in original form ZZZ

**ABSTRACT**

Abundances of primordial, light elements are sensitive to the physics of the early Universe and can directly constrain model parameters, such as the baryon-to-photon ratio $\eta_{10}$, the baryonic density or the number of neutrino families. Deuterium is especially suited for these cosmological studies: its primordial abundance is sensitive and monotonically dependent on $\eta_{10}$ and allows an independent measurement of the cosmic baryon density that can be compared, for instance, against the Planck satellite data. The primordial deuterium abundance can be measured in high HI column density absorption systems towards distant quasars. We report here a new measurement, based on high-resolution ESPRESSO data, of the primordial DI abundance of a system at redshift $z \sim 3.572$, towards PKS1937-101. Using only ESPRESSO data, we find a D/H ratio of $(2.664 \pm 0.091) \times 10^{-5}$, while including available UVES data and fitting the model improves the precision of the estimate, leading to a ratio of $(2.650 \pm 0.074) \times 10^{-5}$. The results of this analysis agree with those of the most precise existing measurements. We find that the relatively low column density of this system ($\log N_{\rm HI} \sim 18$) introduces modelling uncertainties, in turn becoming the main contributors to the error budget.

**Key words:** nuclear reactions, nucleosynthesis, abundances – quasars: absorption lines – primordial nucleosynthesis

## 1 INTRODUCTION

The current standard cosmological model is remarkably able to describe our Universe from a few seconds after the Big Bang to the present day. Despite this, persistent issues have yet to be solved: we do not understand the nature of Dark Energy and Dark Matter, and tensions in the determination of key cosmological parameters have emerged (see e.g., Abdalla et al. 2022).

Investigating the early Universe can offer additional clues to the puzzle. A powerful probe of the physics of the early universe is the Big Bang Nucleosynthesis (BBN), during which light elements (H, D, He3, He4, Li7) were produced (see e.g., Cyburt et al. 2016; Fields et al. 2020). The abundances of these light elements are sensitive to the physics of the early Universe and to the model parameters: the number

★ E-mail: francesco.guarneri@eso.org
Based on observations collected at the European Southern Observatory, Chile, under the programme 0103.A-0512(A).

of neutrino families, for instance, can be constrained by measuring the He abundance (see, e.g., Peimbert et al. 2016). A second primordial element accessible with current facilities is deuterium. Its abundance is of particular interest because it depends monotonically on the baryon-to-photon ratio and, as a consequence, on the baryon density (for a general review on the Big Bang Nucleosynthesis, see e.g., Cyburt et al. 2016; Mathews et al. 2017; Fields et al. 2020; Workman et al. 2022, chapter 24 (Fields, Molaro, Sarkar)). The primordial deuterium abundance is measured by exploiting absorption lines seen in the spectrum of a background source, most commonly a quasar, and computed under the assumption that D/H = $N_{D_I}/N_{H_I}$. As discussed in Cooke et al. (2018, and references therein), there are processes that could weaken this assumption, including the astration of deuterium as gas is cycled through the generation of stars, the relative reionization of hydrogen and deuterium, or the depletion of deuterium onto dust grains. The first two effects are expected to be one order of magnitude below the uncertainties of current measurements at low metallicities. For the third, the amount of dust is small for systems in which deuterium is measured (Workman et al. 2022). A handful of systems at $z \sim 2.5 - 3.0$ have been analysed since 1996, and the Precision Sample presented by Cooke et al. (2018) provides a determination at the 1% level.

As discussed in Cooke et al. (2014, 2018), the best systems for measuring the primordial deuterium abundance are those with HI column density near the threshold of a Damped Ly$\alpha$ system (DLA, log(N) $\sim$ 20.3). In this case the Lorenzian damped wings allow to precisely constrain the total HI column density, while unsaturated DI lines provide a robust measurement of the total DI column density. Unfortunately, DLA systems showing clear DI absorption are rare: only a few are known to date. Lower column density systems ($\log N_H \sim 3\times10^{17} - 1\times10^{19}$) are more common (Riemer-Sørensen et al. 2017, hereafter RS17), but larger uncertainties are associated with the determination of the total HI column density.

In the following, we report of a new measurement of DI/HI in the absorption system at redshift $z = 3.572$ toward PKS1937-101 (J2000 19:39:57.26 -10:02:41.5, $z_{em} = 3.787$, hereafter PKS1937-101) based on recent ESPRESSO data, with higher signal-to-noise ratio and resolution compared to previous data sets. This system is peculiar due to the low metallicity ($Z/Z_\odot \lesssim -2$), relatively low column density, and high redshift. Previous work, based on UVES and HIRES spectra (Riemer-Sørensen et al. 2017) reported a value of DI/HI = $(2.620 \pm 0.051) \times 10^{-5}$.

All PKS1937-101 data sets have been collected using the HIRES (Vogt et al. 1994) and UVES (Dekker et al. 2000) spectrographs. Both instruments have been shown to suffer from wavelength calibration issues (Whitmore & Murphy 2015), causing long-range wavelength scale distortions of ±200 m s$^{-1}$. To account for this, a new spectrum of PKS 1937-101 was collected in 2018 with the Echelle SPectrograph for Rocky Exoplanet and Stable Spectroscopic Observations (Pepe et al. 2021). ESPRESSO's wavelength calibration is significantly better than UVES and HIRES (Schmidt et al. 2021), and the higher resolution allows to better resolve the velocity structure of the system. In addition, the extended wavelength coverage (380-780 nm) compared to previous HIRES and UVES spectra (~400-660, ~380-680 nm respectively) helps identify interlopers and systems that could contaminate the DI and HI lines, revealing previously overlooked systematics.

The paper is organised as follows: in Sect. 2 we describe the data collection and reduction; in Sect. 3 we describe the analysis of the data, the resulting DI/HI ratio, and uncertainties in the modelling of the data. In Sect. 4, archival datasets are included in the analyses while in Sect. 5 we describe a Cloudy model of the system. In Sect. 6, we discuss the present result with respect to other measurements; finally, conclusions are drawn in Sect. 7.

| Observing time (UTC) | Exp. time (s) | S/N (pix$^{-1}$) |
|---|---|---|
| 2019-08-21T23:30:03.725 | 3600 | 20 |
| 2019-08-22T00:41:08.617 | 4100 | 25 |
| 2019-08-22T01:50:11.649 | 4100 | 28 |
| 2019-08-22T02:59:15.783 | 3600 | 28 |
| 2019-08-22T04:13:54.673 | 2400 | 22 |

**Table 1.** The final spectrum used for the analysis consists of five combined exposures. We summarise here relevant information. The S/N column represents the median of the signal to noise ratio along the spectrum.

## 2 OBSERVATIONS AND DATA REDUCTION

PKS1937-101 is a bright ($V_{mag}$ = 16.7) quasar at redshift 3.787. It was observed for the ESPRESSO consortium guaranteed time observation (GTO) in August 2019 for a total of 17800 seconds spread over 5 exposures (see Table 2). All exposures were taken during the same night.

ESPRESSO can be fed by any of the four Unit Telescopes (UTs) of the VLT or by all four telescopes simultaneously. The latter configuration (4-UT mo), equivalent to a 16m telescope in area, was chosen. The exposures were all taken with the 4-UT mode, 8-pixel binning along the spatial direction and 4-pixel binning along the spectral direction (the so-called 'multi-MR84'), providing a nominal resolution of ~ 70000 and a wavelength coverage from 380 nm to 780 nm.

Data were reduced using the standard ESO ESPRESSO data reduction software (DRS) version 3.0.0. We summarise the relevant steps and refer the interested reader to Pepe et al. (2021) for more details. The main steps performed are: i) bias, dark and inter-order background subtraction; ii) optimal extraction, using a modified version of the Zechmeister et al. (2014) algorithm; iii) creation of extracted spectra, with associated error and quality maps; iv) flat fielding and de-blazing; v) wavelength calibration, using either Laser Frequency Comb (LFC, calibration chosen for this work) or Thorium-Argon lamps combined with Fabry-Pérot sources; vi) extraction of the sky spectrum, and creation of a sky-subtracted 2D spectrum. The sky signal was subtracted using the smoothing recipe of the ESPRESSO DRS pipeline.

The five wavelength-calibrated frames were combined using the python software package Astrocook (Cupani et al. 2020), resulting in a spectrum with a signal-to-noise ratio per km s$^{-1}$ of around 100 redward of the Lyman $\alpha$ (Ly $\alpha$) emission line, and from ~ 30 to ~ 90 in the Ly$\alpha$ forest (Fig. 1, bottom panel). The spectrum was rebinned to a wavelength grid with pixels that are constant in velocity space, with pixel size corresponding to 1.4 km s$^{-1}$, providing a 3-pixel sampling of the FWHM of the resolution element at resolution ~ 70000.

Astrocook was also used to fit a continuum to the spectrum. The recipe estimates the continuum by applying an iterative sigma-clipping procedure to remove absorption features, while masking emission lines. The continuum is then computed as the average, unclipped flux, and smoothed in velocity space with a Gaussian filter (FWHM = 200 km s$^{-1}$). This produces reliable results redward of the Ly$\alpha$ emission, where absorption lines are generally narrow and sparse. On the other hand, on the blue side of the Ly$\alpha$ emission line, the recipe systematically underestimates the continuum. We thus manually corrected the continuum level where deemed necessary. We note that this is a subjective but repeatable process owing

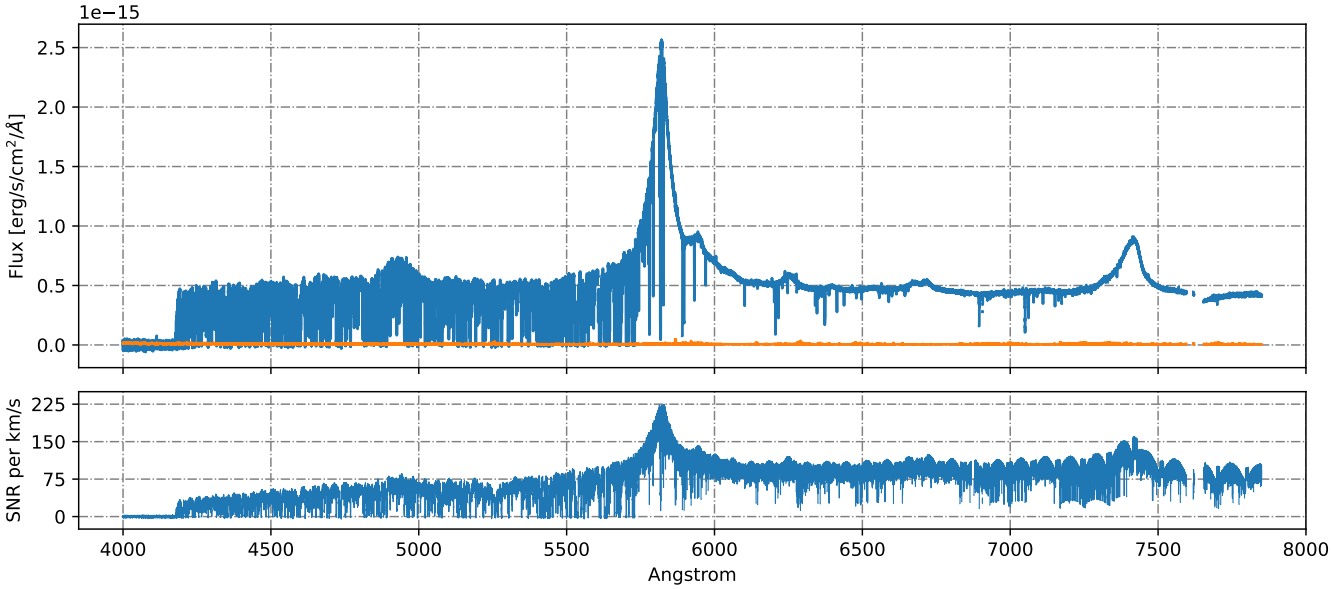


**Figure 1.** Top panel: wavelength calibrated ESPRESSO spectrum of PKS1937-101. The blue line represents the flux, while the orange line represents the associated error. Bottom panel: signal-to-noise ratio per km s$^{-1}$ along the spectrum.

to the capabilities of Astrocook. We briefly discuss the effect of continuum placement on the line fit in Sect. 3.3.5.

## 3 DATA ANALYSIS

We fit the absorption lines of the system at $z \sim 3.572$ using VPFIT (Carswell & Webb 2014). VPFIT is a software package used for Voigt profile fitting of absorption spectra. Each Voigt profile is parameterised by an atomic species, with corresponding atomic parameters, and four free parameters. Atomic parameters (such as laboratory wavelength and oscillator strength) are provided within the VPFIT package, and are a compilation of several literature sources. The free parameters are the redshift of the absorber, $z$, its column density, generally expressed as $\log(N)$[1], and two parameters describing the line broadening $b$ (km s$^{-1}$): one accounting for the turbulent broadening, and one that accounts for thermal broadening. The relation between the broadening parameters is:

$$b_{\rm tot}^2 = b_{\rm turb}^2 + b_{\rm ther}^2 = b_{\rm turb}^2 + \frac{2kT}{m} \quad (1)$$

where $k$ is the Boltzmann constant, $T$ is the temperature of the gas and $m$ is the mass of the atomic species of interest. $b_{\rm turb}$ describes a possible turbulent component of the gas. Provided with a user-supplied model, VPFIT optimises the free parameters using nonlinear least squares minimisation. It then reports the best-fit value for the free parameters, the corresponding errors, the $\chi^2$ and the reduced $\chi^2_\nu$ (i.e., the $\chi^2$ divided by the number of degrees of freedom). While building the model, changes were made only based on $\chi^2_\nu$ (that is, a component was added or removed only if it was deemed necessary to lower the $\chi^2_\nu$ of the fit).

VPFIT also requires information about the instrumental profile, which is convolved with the intrinsic line profile in the observed spectrum. Here it is assumed to be a Gaussian, with a full width at half maximum of 4.28 km s$^{-1}$, corresponding to the nominal resolution of the adopted ESPRESSO configuration.

Due to the large width and saturation of the HI line of the studied system, it is difficult to accurately identify its velocity structure and the number of components needed to carry out a proper fit. On the other hand, metal lines are, for this system, easier to model: they are unsaturated and narrower than the Lyman $\alpha$ profiles. We assumed that low-ionisation metal species share the same velocity structure and absorption components as hydrogen, and use this to model the saturated HI line. In practise, this is equivalent to tying the redshift and Doppler parameters of deuterium and hydrogen to those inferred from the metal lines.

### 3.1 Metal absorption lines

Starting from the metal lines detected in the studied system by RS17, we searched the ESPRESSO spectrum for all associated ionic transitions. Thanks to the extended wavelength range of the ESPRESSO spectrum, we could also detect the SiII 1526 Å and the CIV doublet at 1548, 1550 Å. We considered for our model 6 low ionisation transitions: CII 1334 Å, SiII 1193 Å, SiII 1260 Å, SiII 1304 Å, SiII 1526 Å and FeIII 1122 Å.

Additional metal absorption lines (namely, CIII 977 Å, SiIII 1206 Å, CIV 1548, 1550 Å and SiIV 1393, 1402 Å) are visible in the spectrum, but were not included in the model. CIII and SiIII are in the Lyman forest, where, for both lines, interlopers affect the velocity profile. High-ionisation metals, such as CIV and SiIV, may not share the same velocity structure as low-ionisation species. However, we checked and confirmed that the components found for the other metals were consistent with the CIII, CIV and SiIII, SiIV absorption.

Finally, some commonly found metal transitions, such as OI 1302 Å, are not clearly visible in the spectrum or are heavily contaminated by telluric lines (e.g., AlII 1670 Å). Forcing the presence of OI 1302 Å, while fitting for other metal lines, returns a nonzero summed column density equal to $\log N_{\rm OI} = 12.1 \pm 0.1$. This value is consistent

[1] To simplify the notation, throughout the paper we use $\log(N)$ in place of $\log_{10}(N/{\rm cm}^{-2})$

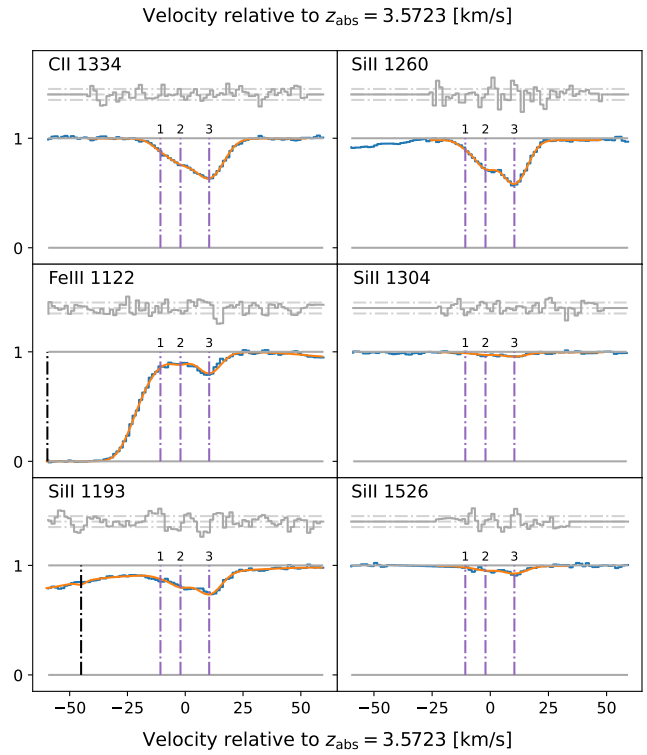


**Figure 2.** Low ionisation metal lines used in the model to constrain the velocity structure of the hydrogen at the same redshift. Absorption components are marked with purple vertical lines, and the three components comprising the model are visible in, e.g., the CII or SiII 1260 Å lines. Black lines mark the position of unrelated HI absorption systems, while the grey line are the normalised residuals (data-model)/error, and the horizontal grey dot-dashed line are the 1-$\sigma$ limits.

with the previous determination of RS17, obtained under slightly different hypothesis, suggesting that the column density determination for OI 1302 Å is a reliable upper limit (we consider this value as an upper limit as these lines are not detected in the spectrum and are force-fitted using VPFIT based on knowledge of the position of the other metal transitions).

We initially only consider metal lines and produce a model of the six listed transitions. Three velocity components, marked 1, 2, 3 in Fig. 2, are needed.

### 3.2 Determination of the Deuterium abundance

We applied the model derived from metal species to HI and DI. An additional line is visible blue-ward of the main HI absorption in the Ly$\alpha$, Ly$\beta$, and Ly$\gamma$ lines (Fig. 4). There are strong indications that this line arises from DI absorption: i) it is significantly broader than other metal lines seen in the spectrum but narrower than the associated Lyman series absorption; ii) the shift between this line and the main HI absorption is $\sim -82\,\mathrm{km\,s^{-1}}$, consistent with the expected shift between DI and HI.

We assumed that low-ionisation metals, hydrogen and deuterium share the same number of components, redshift and Doppler broadening. Column densities were instead free to vary independently. We fit low ionisation metal lines together with the Lyman series (Ly$\alpha$ to Ly9) and the corresponding deuterium series. In order to achieve a more accurate estimate of the total column density of HI and DI, we solved for their respective summed column densities across the absorption system (i.e., we directly found the summed column density for all components of the model). We forced all sub-components to have the same DI/HI ratio (an hypothesis commonly assumed; see, e.g., Cooke et al. (2018)): this implicitly assumes that DI depletion, if present, affects equally all subcomponents.

Several regions require additional unrelated HI absorbers to obtain a good fit. When possible, these are modelled as Lyman $\beta$ or Lyman $\gamma$ lines with an associated Lyman$\alpha$ transition at a longer wavelength. This provides more robust constraints on the number, column density, and position of these lines compared to the use of only Lyman$\alpha$.

We have not explicitly fit transitions higher than the Lyman 9, albeit visible in the spectrum, because the placement of the continuum is uncertain and several interlopers make it difficult to separate the contribution from the main system and unrelated ones. However, we checked that our model does not produce obvious defects when superimposed on those transitions. In Fig. 3, we plot the model and the ESPRESSO spectrum for the Lyman series from Lyman 10 to 20. The two are visually consistent with each other.

Finally, we fit the model to the data and determine the column densities of HI and DI finding $\log(N_{HI}) = 17.921 \pm 0.012$, $\log(N_{DI}) = 13.3471 \pm 0.0084$ and a DI/HI ratio of $(2.664 \pm 0.091) \times 10^{-5}$. The temperature of the gas, averaged across the three components, is $1.77 \times 10^4$ K. We report in Tab. A1 and A2 all relevant parameters for all components.

### 3.3 Modelling uncertainty

We now explore various systematic effects that may have affected our measurements.

#### *3.3.1 Higher excitation metal lines*

Additional lines are available in the spectrum, besides those considered in the modelling: the CIII 977, SiIII 1206, SiIV and CIV doublets. We check that our model is consistent with these absorption systems, finding that extra components are needed to model these lines.

- **SiIV, CIV**: RS17 include SiIV in the fitting model for HI and DI, despite the differences in the ionisation potential. Following their approach, we check if the three-component model is adequate to describe the SiIV and the CIV doublets.

We found that two more components were required to describe the absorption lines. One of these, marked 4 in Fig. 5, is similar to the fourth component found by RS17. The components marked as 5, on the other hand, was previously not identified as part of the absorption system due to lack of wavelength coverage in the UVES and HIRES spectra. These two components are not visible in any of the lower-ionisation metal lines at the same redshift, supporting the hypothesis that high-ionisation lines have a different velocity structure and the choice of not including them in the fit model for hydrogen and deuterium.

- **CIII 977, SiIII 1206 Å**: The three components present in all metal transitions can account for the strong absorption trough seen in Fig. 5. However, both lines are saturated and fall in the Lyman forest, and thus are likely contaminated by HI lines. This is true especially for SiIII, which shows a strong absorption trough that is not evident in any other metal line. Interpreting the velocity structure of CIII is harder: the absorption to the left and right of the strong trough seen in Fig. 5 can either be associated to the fifth component discussed in the previous bullet point or to an additional component,

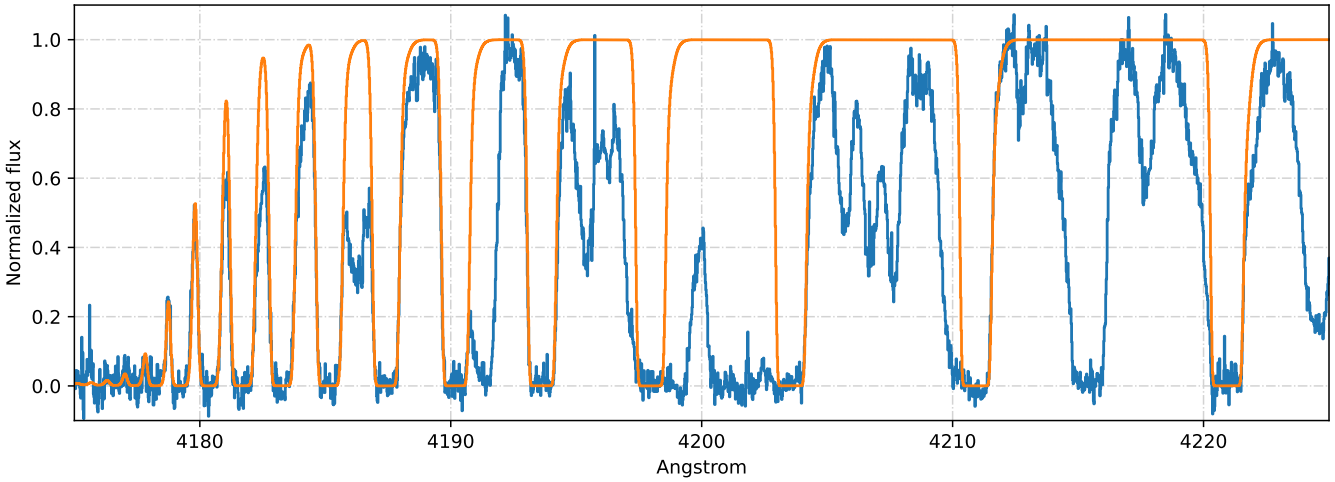


**Figure 3.** ESPRESSO model (orange line) over-plotted onto the high order HI Lyman series lines, from Lyman 10 to Lyman 20 (blue line). The model appears to be consistent with the data.

marked by the number 6 in Fig. 5, to HI interlopers, or to a mix of both.

### 3.3.2 *A model with four components*

RS17 present a model that comprises four components (see, e.g., Fig. 1 of this reference). However, our model considers only three components. We found that a fourth component is only required to adequately fit the SiIV doublet. In the SiII, CII, and FeIII transitions, VPFIT rejects the fourth component entirely. The HI lines are saturated at the tentative location of the fourth component, so HI lines were not considered as they do not provide additional constraints. We interpret this result as confirmation that, for low ionisation species, this component is not necessary. Moreover, the final DI/HI ratio is nearly unchanged with respect to the result found in RS17. We attribute this result to the fact that component 4 is the weakest among the four.

### 3.3.3 *Contamination of HI lines in the Lyman α region*

Contamination by hydrogen interlopers in regions with deuterium absorption is possible, albeit unlikely ($< 3.7\%$, as discussed in RS17). Nonetheless, we investigate how the inclusion of an additional line in the DI region affects the results. We artificially introduce an additional hydrogen component ($\log \mathrm{N} = 12.5$, $b = 10$, $z = 3.57085$) in the region of the DI absorption lines and re-fit the model. This does not lead to significant changes in the final value of $\chi^2_\nu$, which increases by less than 1%, but affects the final DI/HI ratio and significantly increases the uncertainty of the measurement. The best fitting value increases from $(2.664 \pm 0.091) \times 10^{-5}$ to $(2.85 \pm 0.23) \times 10^{-5}$.

### 3.3.4 *Choice of the fitting region*

An additional source of uncertainty is related to the choice of the fitting region, combined with the inclusion of continuum adjustments allowed by the VPFIT model. In particular, considering the Ly$\alpha$ region, we find that restricting the fitting region to $\pm 400$ km s$^{-1}$ (Fig. 4, upper panel) leads to a lower HI column density, $\log(N) = 17.905 \pm 0.023$ and consequently to a higher DI/HI ratio $(2.76 \pm 0.16) \times 10^{-5}$. This is caused by the exclusion of regions where the unabsorbed continuum is higher than in the $\pm 400$ km s$^{-1}$ range: while fitting the model, VPFIT adjusts the continuum to be lower. While possible, it is unlikely that this is the case, as it would require the continuum to change on small scales.

It is interesting to note that both investigated systematics have the effect of raising the value of deuterium over hydrogen for this system.

### 3.3.5 *Continuum placement*

To quantify the effect of the continuum position on the final DI/HI ratio, we randomly varied the placement of the continuum and re-fit the model on the newly normalised spectra. Ten different realisations were produced. To produce each realisation, we multiplied the continuum of the spectrum by a slowly varying function, generated by extracting points from a Gaussian distribution centred on one and with $\sigma = 0.05$. Each point was associated with a wavelength, using a range from 3000Å to 8000Å and a step of 50Å. Finally, points where interpolated with a smoothing spline, then evaluated on the same wavelength scale of ESPRESSO. The model presented in the previous sections was finally fitted separately to each of the ten realisations. We computed the DI/HI ratio for each realisation: their average is $(2.652 \pm 0.029) \times 10^{-5}$, where the error is taken as the standard deviation of the ten iterations. The mean error (that is, the average of the errors estimated from the ten iterations) is 0.0914.

## 4 INCLUDING PREVIOUS DATASETS: UVES AND HIRES

PKS1937 had also been observed with the HIRES and UVES spectrographs. We have analysed this data trying to see if it could be useful for improving the Deuterium fit.

### 4.1 Archival data

PKS1937 has been observed in 2006 and 2007 with UVES (Dekker et al. 2000), proposal 077.A-0166(A) (P.I. Robert Carswell). During the execution of the programme, the object was observed with a

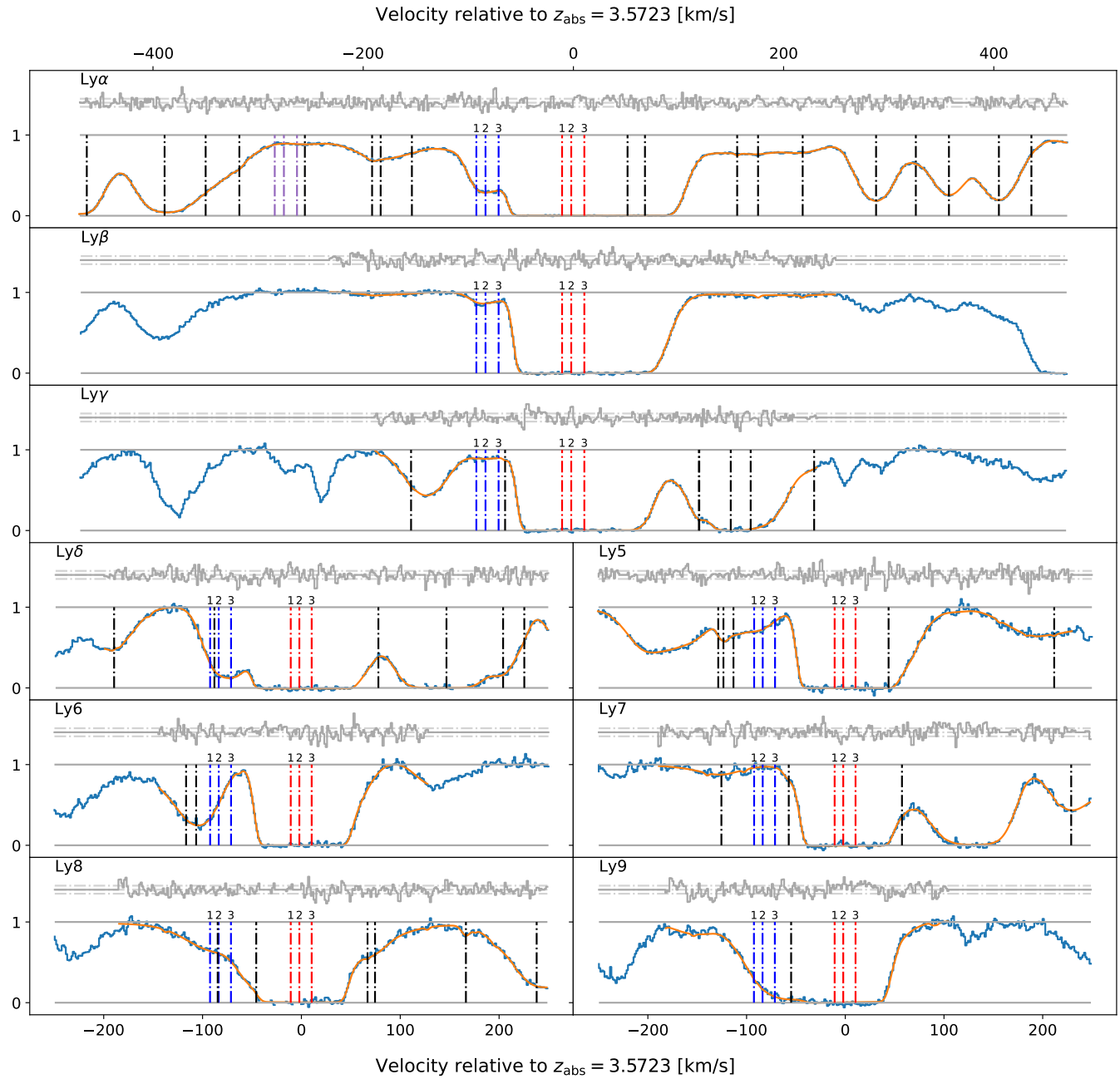


**Figure 4.** Model fitted to the ESPRESSO data only. The blue line shows the spectrum of PKS1937-101, while the orange line shows the model. Residuals are shown above each region, over-plotting the $\pm 1\sigma$ limits. Black dash-dotted lines mark the position of interlopers (i.e., an unrelated HI system along the same line of sight). We only show interlopers added in each region: the remaining absorption is due to Lyman lines at higher redshift. Purple lines in the Lyman $\alpha$ region mark the position of the FeIII at the same redshift of the main system. The red and blue lines mark the positions of the HI and DI components, respectively. Each component of the model is marked with a number (see text).

resolution of R = 45000, for a total of $5.4\times10^4$ seconds spread among 10 individual exposures of $5.4 \times 10^3$ seconds. The spectrum used in this work was taken from the SQUAD dataset (Murphy et al. 2019), a large, public collection of fully reduced, wavelength calibrated QSO spectra observed with UVES. The combined UVES spectrum has roughly half the signal to noise ratio per km s$^{-1}$, compared to the ESPRESSO spectrum, averaging $\sim$ 37 in the Lyman forest and $\sim$ 65 redward of the Ly$\alpha$ emission line. A detailed description of the steps taken to produce the catalogue, reduce each science frame, and produce a stacked spectrum is available in the reference paper.[2]

Science frames were reduced using the ESO Common Pipeline Library and combined using UVES_popler (Murphy 2018). The same tool was also used to fit a continuum on the combined spectrum.

[2] Details of the data processing for all SQUAD QSOs are also available online at the SQUAD web page (github.com/MTMurphy77/UVES_SQUAD_DR1).

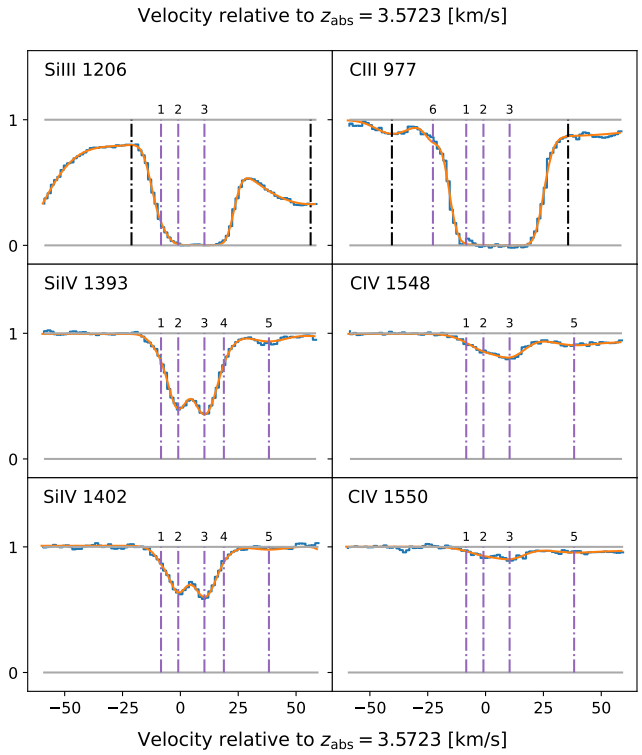


**Figure 5.** Additional metal lines of the system at $z = 3.5723$, not included in the model due to contamination or differences in ionisation potential. As for the other figures, purple lines mark the position of metal lines, numbered on top, while black lines the position of possibly unrelated absorbers, modelled as Lyman $\alpha$.

To do so, data is broken into overlapping chunks of a user-defined width, and a polynomial is fitted on each chunk. To form a smooth continuum, continua from adjacent chunks are averaged together. It should be noted that the automatic procedure does not work well in the Lyman forest, due to the small amount of un-absorbed pixels. For quasars in SQUAD, the continuum in the region of the Lyman forest was manually refitted, selecting seemingly unabsorbed peaks in the Lyman forest and interpolating between them with a low-order polynomial. As for Astrocook, the procedure is subjective but fully repeatable, thanks to UVES_popler log files.

In addition to UVES, PKS1937-101 has been extensively observed using HIRES, mounted on the Keck Telescope in Hawaii. Reduced, wavelength calibrated, and continuum normalised archival data are available as part of the KODIAQ dataset (O'Meara et al. 2021), and were retrieved from SpecDB (Prochaska et al. 2017; Prochaska 2017). Three co-added spectra are available, resulting from observational programmes carried out between 1997 and 2005 (P.I.: L. Cowie, N. Crighton, and D. Tytler). We refer the interested reader to the KODIAQ paper (O'Meara et al. 2021) for details about data reduction and processing.

Out of the three datasets, we noticed wavelength calibration issues in one of the combined spectra (P.I. D. Tytler); we thus discarded it and limited our analysis to the remaining two. The signal to noise per km s$^{-1}$ of the two spectra combined is on average $\sim 40$ in the forest, 60 red-ward of the Lyman $\alpha$ emission line. Finally, it should be noted that the algorithm used to estimate the continuum on HIRES data is again different from the equivalent used for UVES or ESPRESSO spectra. In the case of HIRES, data are continuum normalised on an order-by-order basis by fitting Legendre polynomials (with grade varying from 4th to 12th) in regions deemed free of absorption. Employing three different algorithms might produce different artefacts or systematics in the combined fit.

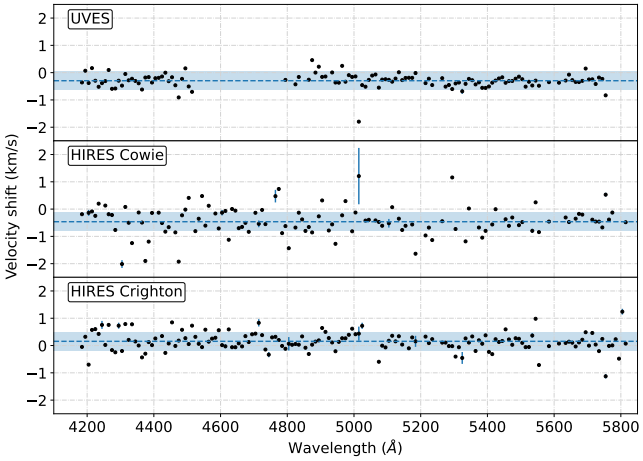


**Figure 6.** Velocity shift between UVES, the two HIRES and ESPRESSO spectra as a function of wavelength. The error-bars on the y-axis represent the scatter in the determination of the velocity shift when computing the cross-correlation from 10 slightly different starting velocity values, equally spaced within a pixel. The adopted shifts, assumed to be constants, are $|v_{\rm shift}| = 0.295$ km s$^{-1}$, 0.463 km s$^{-1}$ and 0.154 km s$^{-1}$ respectively.

### 4.2 ESPRESSO model applied to UVES data

Before fitting the model on UVES data, we attempted to correct some of the known systematics of the UVES spectrum. In particular, we take advantage of the significantly better ESPRESSO wavelength calibration to adjust the wavelength grid of the UVES data. When this is done, multiple spectra can be fitted together.

UVES has been shown to suffer from wavelength calibration issues (e.g., Rahmani et al. 2013). Attempting to fit UVES and ESPRESSO data together should take this into account, either by introducing velocity shifts as free parameters in the fit or computing the shift between ESPRESSO, used as reference, and UVES. We opt for the second choice, and considering the wavelength calibration of ESPRESSO to be precise and accurate, we compute velocity shifts along the entire spectrum of UVES with respect to ESPRESSO data.

This was achieved by cross-correlating the two spectra in the velocity space, which were rebinned to a common velocity grid, with a pixel size of 1.4 km s$^{-1}$. The choice of the pixel size did not affect the resulting shifts, as long as it is not too large ($> 4.5$ km s$^{-1}$). The two spectra are then subdivided into chunks, and each pair of corresponding chunks is cross-correlated with each other. We compute the cross-correlation considering relative shifts between -5 and 5 km s$^{-1}$, with a fixed step of $10^{-3}$ km s$^{-1}$. The velocity shift corresponding to the maximum of the cross-correlation function is taken as the velocity shift between two chunks.

The shift between UVES and ESPRESSO appears to depend weakly on the wavelength (Fig. 6). Therefore, we assume a single value, taken as the weighted average of the single cross-correlation values we computed for the 10Å window $|v_{\rm shift}| = 0.295$ km s$^{-1}$. This shift is applied to the UVES data as a fixed parameter in the VPFIT input.

Having applied the wavelength scale corrections to the UVES

spectrum, we re-fitted the absorption system model and obtained column densities of $\log N_{\rm HI} = 17.922 \pm 0.026$ and $\log N_{\rm DI} = 13.338 \pm 0.012$, yielding a corresponding DI/HI ratio of $(2.60 \pm 0.17) \times 10^{-5}$, well in agreement with the result based on the ESPRESSO spectrum alone, although with a slightly lower column density.

#### 4.2.1 Fitting together UVES and ESPRESSO data

We also performed a joined fit of the ESPRESSO and UVES data. VPFIT allows different data sets to be fit at the same time, using the same model, without having to resort to stacking or data manipulation techniques.

The resulting column densities, derived from the joined fit as described above, are $\log N_{\rm HI} = 17.922 \pm 0.011$ and $\log N_{\rm DI} = 13.345 \pm 0.006$, leading to an estimate of the deuterium over hydrogen ratio of $(2.650 \pm 0.074) \times 10^{-5}$.

### 4.3 ESPRESSO model, applied on HIRES

The HIRES data were corrected in an analogous way as UVES data were. We then performed a joint fit of the ESPRESSO, UVES, and HIRES data.

Interestingly, despite the increase in S/N achieved by including additional data ($\sim 10\%$ compared to the combination of ESPRESSO and UVES data), we find slightly larger errors in the HI and DI column densities compared to the joint fit in ESPRESSO and UVES. The values returned by the fit are: $\log N_{\rm HI} = 17.916 \pm 0.013$, $\log N_{\rm DI} = 13.348 \pm 0.008$, DI/HI $= (2.70 \pm 0.09) \times 10^{-5}$.

The higher uncertainty can be attributed to several factors, including different normalisations for each spectra or region-dependent wavelength shifts (see Sect. 6.2). In the following, we will consider the combined ESPRESSO + UVES value.

## 5 CLOUDY MODEL OF THE SYSTEM

We use Cloudy (Ferland et al. 2017) to estimate the metallicity of the system, the temperature of the absorber and the hydrogen density. Cloudy is a spectral synthesis code designed to simulate astrophysical environments and predict their spectra. Given the presence in the spectrum of several transitions with different ionisation stages, we use the `optimize` function to estimate the temperature, hydrogen density, and metallicity of the system.

We assume the gas to be in photoionisation equilibrium with the ultraviolet ionising background. We chose the HM12 option, i.e. an isotropic ionising background with the contribution of both quasars and galaxies, with a variable escape fraction $\langle f_{\rm esc} \rangle$ depending on the redshift of interest (Haardt & Madau 2012). The contribution of the CMB, although negligible, is also taken into account. We approximate the absorption systems as a plane parallel slab with hydrogen density $n_{\rm H}$ cm$^{-3}$ and metallicity $Z/Z_\odot$: these two quantities are free parameters, and the best-fit value will be estimated by Cloudy during the optimisation process. We allow the optimiser to explore a reasonably large range for both quantities: the allowed interval for the hydrogen density is $-5 < n_H\ [\rm cm^{-3}] < 2$, for metallicity $-3 < Z/Z_\odot < 0$. We use the median point as initial guesses for each interval. We also note that both initial guesses and allowed ranges are consistent with values found in the literature.

Table 2 reports the Cloudy output. The simulated column densities are generally consistent with those estimated by the fit. The most obvious exception to this is FeIII, which appears to have significantly higher column density in our VPFIT model. This can be explained by the fact that the FeIII lines lie in the Lyman forest and, as such, might be affected by Lyman $\alpha$ interlopers or imperfect continuum placement.

| Metal species | Cloudy | Fit |
|---|---|---|
| CII | 13.38 | $13.35 \pm 0.06$ |
| CIII* | 14.44 | <14.25 |
| CIV | 12.88 | $13.01 \pm 0.14$ |
| SiII | 12.45 | $12.42 \pm 0.07$ |
| SiIII* | 13.53 | <13.90 |
| SiIV | 12.79 | $13.10 \pm 0.10$ |
| FeIII* | 12.80 | <13.33 |
| OI* | 11.23 | <12.10 |
| $n_H$ [cm$^{-3}$] | -2.49 | |
| $Z/Z_\odot$ | -2.45 | |

**Table 2.** Results of the optimisation process from Cloudy, and inferred column densities from the modelling. Metal species marked with * are formally upper limits, either because column densities were determined by force-fitting absorption lines at the position of the absorber (in the case of OI), or the lines are in the Lyman forest, and as such a part of the absorption can be attributed to Lyman $\alpha$ interlopers (everything else).

The estimated hydrogen density for the cloud, $n_H$ [cm$^{-3}$], is lower (by a factor of 3) than the minimum value determined by RS17, who compared the column density ratios observed with a grid of Cloudy models and estimated it to be $-2.11 < n_H\ [\rm cm^{-3}] < -1.72$. The best estimate of metallicity is consistent with previous determinations ($-2.5 < Z/Z_\odot < -1.99$, RS17) and recent analysis of low-metallicity systems (Lofthouse et al. 2023). We note that our simulation uses an updated UV background with respect to RS17: re-running the model using the HM05 UV background, same as RS17, yields $n_H\ [\rm cm^{-3}] = -2.27$, closer to the lower limit found by RS17. Finally, we obtain an average temperature for the system of $1.76 \cdot 10^4$K, in good agreement with the temperature estimated by VPFIT.

## 6 DISCUSSION

Inferring the HI column density is an inherently difficult task and various authors have reported different values for this absorption system, with inconsistent conclusions. Tytler et al. (1996) found a value of $\log N_{\rm H_I} = 17.94 \pm 0.3 \pm 0.3$ cm$^{-2}$, where the first error is statistical and the second is systematic. The estimate was subsequently revised to $\log N_{\rm H_I} = 17.86 \pm 0.02$ cm$^{-2}$ based on the LRIS, HIRES and Kast data (Burles & Tytler 1997). Improvement in the determination was achieved by developing a new method to estimate the HI column density from the Lyman continuum optical depth. This result was however inconsistent with results from Songaila et al. (1997, $\log N_{\rm HI} < 17.7$ cm$^{-2}$) or Wampler (1996), who again estimated a lower $\log N_{\rm HI}$ column density.

In addition to measurements of the HI column density, PKS1937-101 has three previous determinations of the D/H ratio (Tytler et al. 1996; Burles & Tytler 1998; Riemer-Sørensen et al. 2017). Tytler et al. (1996) estimated a D/H ratio of $(2.3 \pm 0.3) \times 10^{-5}$, while improvements in the determination of HI from Burles & Tytler (1998) lead to an updated value of $(3.3 \pm 0.3) \times 10^{-5}$. However, in their analysis, metal components were not used to better constrain the velocity structure of the system. Instead, the position and the number of components for DI and HI are only constrained using Lyman lines. The discrepancy between their final determination and the value presented in this paper is due to the different HI column density,

lower in Burles & Tytler (1998) than the present measurement (Tab. 3).

More recently, the system has been revisited by RS17, who used data from Keck/LRIS, Keck/HIRES and VLT/UVES. They report a value of the primordial deuterium over hydrogen ratio of $(2.620 \pm 0.051) \times 10^{-5}$. Their determination of D/H is consistent and within $1\sigma$ of the one presented in this paper, albeit with smaller uncertainties. There are, however, some differences: our model does not include high-ionisation metal species, which might not faithfully trace the HI velocity structure, leading to a three-component model (Sect. 3.3.2 shows how including a fourth component is only required to adequately fit the SiIV doublet). In addition to this, in this work interlopers are modelled, when possible, as Ly$\beta$ or Ly$\gamma$ lines with an associated Ly$\alpha$ line at a longer wavelength, instead of simple Ly$\alpha$; this should make the model more robust, as interlopers are constrained more precisely. We also note that the determination from the ESPRESSO data, even when combined with UVES, leads to a slightly larger uncertainty than RS17. We show that systematic uncertainties are significant (Sect. 3.3), and as such that the errors in previous analyses might be underestimated. Simply taking the smallest systematic uncertainty identified in this work as also representative of the joint ESPRESSO-UVES fit increases the error by $\sim 7\%$, from 0.074 to $\sqrt{0.074^2 + 0.029^2} = 0.079$.

### 6.1 Determinations of D/H from other systems in the literature.

We compare the determination presented in this work against the determinations from other systems, including the Precision Sample defined by Cooke et al. (2018).

In Table 4, we report the "robust" D/H measurements initially selected by Pettini et al. (2008) and updated in subsequent articles (RS15, RS17, Zavarygin et al. (2018)) with the new determination derived in this paper for the system at z=3.572 in PKS1937-101. Values from the same table are plotted in Fig. 7.

Qualitatively, there is no apparent correlation between redshift, metallicity, column density of the absorber and the D/H ratio. In particular, the absence of correlation with redshift strengthens the result by Cooke et al. (2018) since the updated sample spans a wider redshift range.

The collection presented in this section is inhomogeneous and includes results obtained with different hypotheses (for example, Noterdaeme et al. (2012); Balashev et al. (2016) assume a constant ratio of OI/HI across all components of the system, Cooke et al. (2018) allow the temperature of hydrogen and deuterium to vary independently). Averaging all the measurements reported in Tab. 4, we find simple and weighted averages of $(2.32 \pm 0.40) \times 10^{-5}$ and $(2.534 \pm 0.025) \times 10^{-5}$, respectively. As expected, the weighted average is consistent with the results of Cooke et al. (2018), as 7 out of 16 measurements in Tab. 4 are also in the Precision Sample. These also have the smallest formal errors, so it is expected that the weighted average of all 16 measurements in Tab. 4 is close to the Precision Sample average. The simple average, on the other hand, is lower and inconsistent with the value provided by the Precision Sample at the level of $\sim 2\sigma$. This is due to the measurements with very discrepant lower values, which, however, also have larger error bars, and in general to the fact that the sample has not been analysed homogeneously. Taking into account only measurements with an error estimate lower than 10% the simple mean results in $(2.53 \pm 0.09) \times 10^{-5}$, while the weighted average is almost unchanged $(2.550 \pm 0.025) \times 10^{-5}$.

On the other hand, comparing against the Precision Sample, for which Cooke et al. (2018) report a determination of the primordial deuterium abundance of $(2.527 \pm 0.030) \times 10^{-5}$, we find that the result from ESPRESSO data alone is in agreement as is the one obtained with the combination of ESPRESSO and UVES data, at the $\sim 1.6\sigma$ level.

Finally, we compare the new determination with the most recent results from the Planck Collaboration (Planck Collaboration et al. 2020). Converting CMB data to deuterium abundance requires prior knowledge of nuclear reaction rates, and the Planck Collaboration presents three possibilities (D/H = $2.587 \pm 0.130$, $2.455 \pm 0.081$, $2.439 \pm 0.082$), depending on the nuclear reaction rates considered. The combined ESPRESSO and UVES measurement agrees with these results at $0.4\sigma$, $1.8\sigma$ and $1.9\sigma$, respectively (Fig. 7). More recently, the LUNA experiment updated the cross-section of the deuterium burning D$(p,\gamma)^3$He reaction (Mossa et al. 2020) and provided a new determination of D/H of $2.52 \pm 0.03 \pm 0.06 \times 10^{-5}$, in agreement with the determination of this work at the $1.3\sigma$ level (Fig. 8). Thus, no significant tension is found, even if the offset in the central value suggests that systematic uncertainties for this system might be underestimated.

### 6.2 About the uncertainty

The results obtained in this analysis have a higher uncertainty than RS17. This is somewhat unexpected, given the higher resolution, signal-to-noise ratio per km s$^{-1}$ and significantly better wavelength calibration of ESPRESSO. We attribute this to two aspects: on one hand, we attempt to fit together spectra from 3 different instruments. On the other hand, comparing the joint UVES and HIRES results with those obtained on single spectra, we recognise an unusual scaling in the final uncertainty reported by RS17.

With respect to the first point, UVES and HIRES have been shown in the past to be affected by systematics in the wavelength calibration. To account for this, we precompute the velocity shift of each fitting region and use the average value as a fixed parameter during the optimisation procedure. This is somewhat unique to this work: in RS17, for instance, a velocity shift between regions is allowed as a free parameter. In addition to this, each spectrum is reduced following slightly different prescriptions, and the continuum is determined with different algorithms. Systematic effects are thus expected and are hard to control. We argue that the increase in the uncertainty in the final measurement simply reflects the increased incompatibility of the input spectra. In support of this, fitting the model on HIRES data alone yields higher (albeit still consistent) DI/HI than ESPRESSO, UVES or the combination of the two (DI/HI$_{\rm HIRES}$ = $(2.89 \pm 0.23) \times 10^{-5}$).

In addition to this, we also note an atypical trend in the scaling of the final uncertainties reported by RS17: the uncertainty when fitting the model on single spectra (either UVES or HIRES) is a factor of three larger than the corresponding value found on the combined fit. Instead, we would expect the error to scale with the square root of the signal-to-noise ratio. This would lead to an uncertainty on the final determination by RS17 of $\sim 0.11$: systematics would further increase this number. This is quantified in Sect. 3.3.5 and Sect. 3.3.4. We find that, for example, the choice of a narrower fitting region combined with continuum adjustments shifts the central value of the DI/HI by nearly one $\sigma$. Based on these arguments, we show that the uncertainty of the determination is higher than previously reported and is likely dominated by systematics rather than statistical uncertainty.

| Publication | log $N_{\rm DI}$ [cm$^{-2}$] | log $N_{\rm HI}$ [cm$^{-2}$] | DI/HI (x $10^{-5}$) |
|---|---|---|---|
| Tytler et al. (1996) | 13.30 ± 0.04 | 17.94 ± 0.05 | 2.3 ± 0.6 |
| Burles & Tytler (1998) | /// | 17.86 ± 0.02 | 3.24 ± 0.30 |
| RS17 (UVES) | 13.3320 ± 0.0287 | 17.9250 ± 0.0063 | 2.580 ± 0.175 |
| RS17 (HIRES) | 13.3570 ± 0.0244 | 17.9250 ± 0.0066 | 2.700 ± 0.157 |
| RS17 (Combined) | 13.3440 ± 0.0056 | 17.9210 ± 0.0068 | 2.620 ± 0.051 |
| This work (ESPRESSO) | 13.3490 ± 0.0084 | 17.921 ± 0.012 | 2.664 ± 0.091 |
| This work (UVES) | 13.338 ± 0.012 | 17.923 ± 0.026 | 2.60 ± 0.17 |
| This work (HIRES) | 13.357 ± 0.029 | 17.895 ± 0.019 | 2.89 ± 0.23 |
| This work (ESPRESSO + UVES) | 13.3450 ± 0.0060 | 17.922 ± 0.011 | 2.650 ± 0.074 |
| This work (ESPRESSO + HIRES) | 13.3530 ± 0.0079 | 17.910 ± 0.013 | 2.770 ± 0.094 |
| This work (ESPRESSO + UVES + HIRES) | 13.3480 ± 0.0080 | 17.916 ± 0.013 | 2.703 ± 0.093 |

**Table 3.** Summary of the DI/HI measurements for the system at $z = 3.572$ in PKS 1937-101 quoted in the text.

| Reference | Quasar | redshift of the system | log $N_{\rm HI}$ | [X/H] | D/H (x $10^5$) |
|---|---|---|---|---|---|
| Pettini & Bowen (2001) | Q2206-199 | 2.076 | 20.436 ± 0.008 | -2.04 [Si/H] | 1.65 ± 0.35 |
| Kirkman et al. (2003) | Q1243+3047 | 2.426 | 19.70 ± 0.04 | -2.79 [O/H] | 2.43 ± 0.35 |
| Balashev et al. (2016) | J1444+2919 | 2.437 | 19.983 ± 0.010 | -2.04 [O/H] | 1.97 ± 0.33 |
| Zavarygin et al. (2018) | Q1009+2956 | 2.504 | 17.362 ± 0.005 | -2.50 [Si/H] | 2.48 ± 0.41 |
| Cooke et al. (2018)* | Q1243+3047 | 2.525 | 19.761 ± 0.026 | -2.77 [O/H] | 2.39 ± 0.10 |
| O'Meara et al. (2001)* | HS 0105+1619 | 2.536 | 19.40 ± 0.01 | -1.77 [O/H] | 2.58 ± 0.15 |
| Pettini et al. (2008)* | Q0913+072 | 2.618 | 20.312 ± 0.008 | -2.40 [O/H] | 2.53 ± 0.10 |
| Noterdaeme et al. (2012) | J0407-4410 | 2.621 | 20.45 ± 0.10 | -1.99 [O/H] | 2.80 ± 0.80 |
| O'Meara et al. (2006)* | J1558-0031 | 2.702 | 20.75 ± 0.03 | -1.55 [O/H] | 2.40 ± 0.14 |
| Cooke et al. (2016)* | SDSS J1358+0349 | 2.853 | 20.524 ± 0.006 | -2.804 [O/H] | 2.62 ± 0.07 |
| D'Odorico et al. (2001) | QSO 0347-3819 | 3.025 | 20.63 ± 0.09 | -1.25 [Zn/H] | 2.24 ± 0.67 |
| Pettini & Cooke (2012)* | J1419+0829 | 3.049 | 20.392 ± 0.003 | -1.92 [O/H] | 2.51 ± 0.05 |
| Cooke et al. (2014)* | J1358+6522 | 3.067 | 20.50 ± 0.01 | -2.33 [O/H] | 2.58 ± 0.10 |
| Srianand et al. (2010) | J1337+3152 | 3.168 | 20.41 ± 0.15 | -2.68 [Si/H] | 1.2 ± 0.5 |
| Riemer-Sørensen et al. (2015) | Q1937-101 | 3.256 | 18.09 ± 0.03 | -1.87 [O/H] | 2.45 ± 0.28 |
| Fumagalli et al. (2011) | J1134+5742 | 3.411 | 17.95 ± 0.05 | < -4.20 [Si/H] | 2.04 ± 0.61 |
| This work | PKS1937-101 | 3.572 | 17.922 ± 0.023 | -2.52 [O/H] | 2.650 ± 0.074 |

**Table 4.** Collection of measurements of the primordial deuterium abundance from the literature. Starred QSOs are part of the Precision Sample presented in Cooke et al. (2018).

## 7 SUMMARY AND CONCLUSIONS

We have presented a new determination of the abundance of primordial deuterium in an absorption system at redshift $z = 3.572$ seen towards the quasar PKS1937-101. The system was already studied in the past with different instruments (Tytler et al. 1996; Burles & Tytler 1998; Riemer-Sørensen et al. 2017). It is a Lyman limit system ($\log N_{\rm H} \sim 17.9$) showing a clear absorption due to DI at the redshift of the HI Lyman $\alpha$ and Lyman $\beta$ lines. The analysis was carried out using new ESPRESSO data, of higher quality compared to previous measurements based on UVES and HIRES data alone. The new ESPRESSO data have 50% higher S/N per km s$^{-1}$ at almost double spectral resolution and significantly better wavelength calibration. In addition to the analysis of the ESPRESSO data alone, archival data have been included to further reduce the final measurement uncertainties.

Based on ESPRESSO data alone, we found a deuterium over hydrogen ratio of $(2.664 \pm 0.091) \times 10^{-5}$ (Sect. 3.2). This is slightly higher than the most recent measurement by RS17, although consistent within the respective error bars. Including archival UVES data, we found D/H = $(2.650 \pm 0.074) \times 10^{-5}$ (Sect. 4.2), while the inclusion of HIRES data did not decrease the uncertainty, possibly indicating that we have reached the limit of statistical errors (Sect. 4.3 and Sect. 6.2). The systemic effects that may explain this are difficult to model. The determination of the joint ESPRESSO-UVES fit is consistent with the weighted mean presented by Cooke et al. (2018) based on the Precision Sample ($\sim 1.6\sigma$ level), Planck data ($0.4, 1.8, 1.9\sigma$ level, Planck Collaboration et al. 2020), and recent results from the LUNA experiment ($\sim 1.3\sigma$ level, Mossa et al. 2020).

Using ESPRESSO data, we discussed uncertainties in the modelling. We quantified the impact of continuum estimation uncertainties on the final measurement, finding that, while the central value in ten iterations does not change, the standard deviation leads to an uncertainty 7% larger. We investigated whether a fourth component is needed, finding that it is only required to adequately fit higher ionisation lines, but it is removed when considering low-ionisation metals, DI and HI. Furthermore, we found that choosing a smaller fitting region for the Ly$\alpha$ region leads to a higher determination of D/H of $(2.76 \pm 0.16) \times 10^{-5}$: this is due to VPFIT adjusting the continuum to be lower, reducing the HI column density. Our model also fits well the higher-order Lyman series lines.

Surprisingly, the final determination from the ESPRESSO and UVES data carries higher uncertainties than those reported by RS17. Column densities of HI lines in the Lyman limit range ($17.3 \leq \log N_{\rm HI} \leq 19$), as the one analysed here, are hard to constrain precisely because the line is saturated but it is not yet showing the Damped wings of the Lorentzian profile. This is evidenced by the disagreement among independent determinations. Moreover, systematic errors from the continuum placement or the choice of the fitting region are significant.

Finally, we combine the results of this work with a collec-

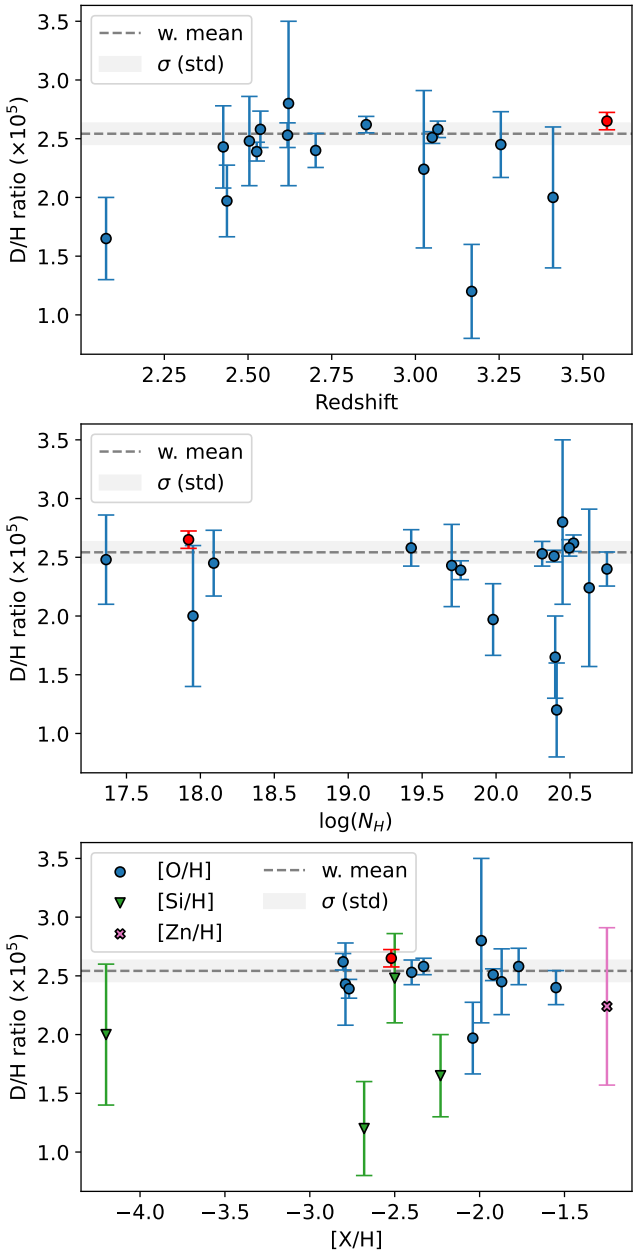


**Figure 7.** Data from Tab. 4, plotted from top to bottom against redshift, HI column density and metallicity of the absorber. The red point is the new measurement reported in this work, the grey, dashed line the weighted mean of measurements in Tab. 4, while the grey shaded regions represent the $1\sigma$ standard deviation. In the third panel, metallicity is estimated through different metal ratios, colour coded according to the legend on the top left. No clear correlations are evident.

tion of results from the literature. A weighted average of the sample leads to D/H=(2.534 ± 0.025) × $10^{-5}$. This changes to D/H=(2.550±0.025)×$10^{-5}$ if we exclude measurements with uncertainties greater than 10%. Considering the whole sample, we do not find any correlation between the D/H ratio and the redshift, metallicity or the column density HI, confirming the findings of Cooke et al. (2018). The results of the combined sample are also consistent with both Planck (Planck Collaboration et al. 2020) and LUNA (Mossa et al. 2020) experiments: no significant tension is evident.

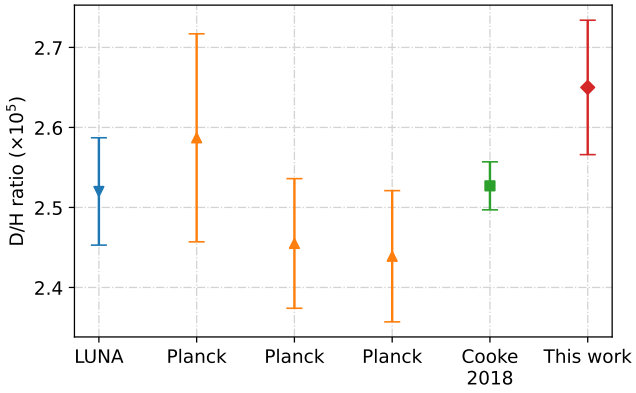


**Figure 8.** Primordial deuterium abundance from the LUNA experiment (Mossa et al. 2020), Planck data and the Precision Sample presented in Cooke et al. (2018), compared to the results of the present work. Planck provides three different measurements, depending on the assumed nuclear rates (Planck Collaboration et al. 2020).

## ACKNOWLEDGEMENTS

The authors acknowledge the ESPRESSO project team for its effort and dedication in building the ESPRESSO instrument. The INAF authors acknowledge the financial support of the Italian Ministry of Education, University, and Research with PRIN 201278X4FL and the "Progetti Premiali" funding scheme. SC and DM are partly supported by the INFN PD51 INDARK grant. JIGH, ASM, CAP and RR acknowledge financial support from the Spanish Ministry of Science and Innovation (MICINN) project PID2020-117493GB-I00. This work was supported by Portuguese funds through FCT - Fundação para a Ciência e a Tecnologia through national funds and in the framework of the project 2022.04048.PTDC, and by FEDER through COMPETE2020 - Programa Operacional Competitividade e Internacionalização by these grants: UIDB/04434/2020; UIDP/04434/2020. CJM also acknowledges FCT and POCH/FSE (EC) support through Investigador FCT Contract 2021.01214.CEECIND/CP1658/CT0001. S.G.S acknowledges the support from FCT through Investigador FCT contract nr. CEECIND/00826/2018 and POPH/FSE (EC). FPE would like to acknowledge the Swiss National Science Foundation (SNSF) for supporting research with ESPRESSO through the SNSF grants nr. 140649, 152721, 166227 and 184618. The ESPRESSO Instrument Project was partially funded through SNSF's FLARE Programme for large infrastructures. TMS acknowledgment the support from the SNF synergia grant CRSII5-193689 (BLUVES) MTM acknowledges the support of the Australian Research Council through Future Fellowship grant FT180100194.

We acknowledge financial support from the Agencia Estatal de Investigación of the Ministerio de Ciencia e Innovación MCIN/AEI/10.13039/501100011033 and the ERDF "A way of making Europe" through project PID2021-125627OB-C32, and from the Centre of Excellence "Severo Ochoa" award to the Instituto de Astrofisica de Canarias.

## DATA AVAILABILITY

The data underlying this article will be shared on reasonable request to the corresponding author.

## REFERENCES


Abdalla E., et al., 2022, Journal of High Energy Astrophysics, 34, 49

Balashev S. A., Zavarygin E. O., Ivanchik A. V., Telikova K. N., Varshalovich D. A., 2016, MNRAS, 458, 2188

Burles S., Tytler D., 1997, AJ, 114, 1330

Burles S., Tytler D., 1998, ApJ, 499, 699

Carswell R. F., Webb J. K., 2014, VPFIT: Voigt profile fitting program, Astrophysics Source Code Library, record ascl:1408.015 (ascl:1408.015)

Cooke R. J., Pettini M., Jorgenson R. A., Murphy M. T., Steidel C. C., 2014, ApJ, 781, 31

Cooke R. J., Pettini M., Nollett K. M., Jorgenson R., 2016, ApJ, 830, 148

Cooke R. J., Pettini M., Steidel C. C., 2018, ApJ, 855, 102

Cupani G., D'Odorico V., Cristiani S., Russo S. A., Calderone G., Taffoni G., 2020, in Guzman J. C., Ibsen J., eds, Vol. 11452, Software and Cyberinfrastructure for Astronomy VI. SPIE, p. 114521U, doi:10.1117/12.2561343, https://doi.org/10.1117/12.2561343

Cyburt R. H., Fields B. D., Olive K. A., Yeh T.-H., 2016, Reviews of Modern Physics, 88, 015004

D'Odorico S., Dessauges-Zavadsky M., Molaro P., 2001, A&A, 368, L21

Dekker H., D'Odorico S., Kaufer A., Delabre B., Kotzlowski H., 2000, in Iye M., Moorwood A. F., eds, Society of Photo-Optical Instrumentation Engineers (SPIE) Conference Series Vol. 4008, Optical and IR Telescope Instrumentation and Detectors. pp 534–545, doi:10.1117/12.395512

Ferland G. J., et al., 2017, Rev. Mex. Astron. Astrofis., 53, 385

Fields B. D., Olive K. A., Yeh T.-H., Young C., 2020, J. Cosmology Astropart. Phys., 2020, 010

Fumagalli M., O'Meara J. M., Prochaska J. X., 2011, Science, 334, 1245

Haardt F., Madau P., 2012, ApJ, 746, 125

Kirkman D., Tytler D., Suzuki N., O'Meara J. M., Lubin D., 2003, ApJS, 149, 1

Lofthouse E. K., et al., 2023, MNRAS, 518, 305

Mathews G. J., Kusakabe M., Kajino T., 2017, International Journal of Modern Physics E, 26, 1741001

Mossa V., et al., 2020, Nature, 587, 210

Murphy M., 2018, MTMurphy77/UVES_popler: UVES_popler: POst-PipeLine Echelle Reduction software, doi:10.5281/zenodo.1297190, https://doi.org/10.5281/zenodo.1297190

Murphy M. T., Kacprzak G. G., Savorgnan G. A. D., Carswell R. F., 2019, MNRAS, 482, 3458

Noterdaeme P., López S., Dumont V., Ledoux C., Molaro P., Petitjean P., 2012, A&A, 542, L33

O'Meara J. M., Tytler D., Kirkman D., Suzuki N., Prochaska J. X., Lubin D., Wolfe A. M., 2001, ApJ, 552, 718

O'Meara J. M., Burles S., Prochaska J. X., Prochter G. E., Bernstein R. A., Burgess K. M., 2006, ApJ, 649, L61

O'Meara J. M., Lehner N., Howk J. C., Prochaska J. X., 2021, AJ, 161, 45

Peimbert A., Peimbert M., Luridiana V., 2016, Rev. Mex. Astron. Astrofis., 52, 419

Pepe F., et al., 2021, A&A, 645, A96

Pettini M., Bowen D. V., 2001, ApJ, 560, 41

Pettini M., Cooke R., 2012, MNRAS, 425, 2477

Pettini M., Zych B. J., Murphy M. T., Lewis A., Steidel C. C., 2008, MNRAS, 391, 1499

Planck Collaboration et al., 2020, A&A, 641, A6

Prochaska J. X., 2017, Astronomy and Computing, 19, 27

Prochaska J. X., Tejos N., jnburchett Lau M. W., jhennawi O'Meara J., 2017, specdb/specdb: First Release, doi:10.5281/zenodo.1069833, https://doi.org/10.5281/zenodo.1069833

Rahmani H., et al., 2013, MNRAS, 435, 861

Riemer-Sørensen S., et al., 2015, MNRAS, 447, 2925

Riemer-Sørensen S., Kotuš S., Webb J. K., Ali K., Dumont V., Murphy M. T., Carswell R. F., 2017, MNRAS, 468, 3239

Schmidt T. M., et al., 2021, A&A, 646, A144

Songaila A., Wampler E. J., Cowie L. L., 1997, Nature, 385, 137

Srianand R., Gupta N., Petitjean P., Noterdaeme P., Ledoux C., 2010, MNRAS, 405, 1888

Tytler D., Fan X.-M., Burles S., 1996, Nature, 381, 207

Vogt S. S., et al., 1994, in Crawford D. L., Craine E. R., eds, Society of Photo-Optical Instrumentation Engineers (SPIE) Conference Series Vol. 2198, Instrumentation in Astronomy VIII. p. 362, doi:10.1117/12.176725

Wampler E. J., 1996, Nature, 383, 308

Whitmore J. B., Murphy M. T., 2015, MNRAS, 447, 446

Workman R. L., et al., 2022, PTEP, 2022, 083C01

Zavarygin E. O., Webb J. K., Dumont V., Riemer-Sørensen S., 2018, MNRAS, 477, 5536

Zechmeister M., Anglada-Escudé G., Reiners A., 2014, A&A, 561, A59

## APPENDIX A: VPFIT MODEL

Table A1: We report for each transition included in the model the corresponding column density, redshift and total $b$ parameter. For the transitions where we fit for both $b_{\rm turb}$ and T we report the error separately for both quantities, and not on the $b_{\rm tot}$. For transitions marked with *, the reported column density is the sum of the column densities across the three components, and only report the error on the sum.

| Transition | N | $\Delta N$ | $z$ | $\Delta z$ | $b_{\rm tot}$ | $\Delta b_{\rm tot}$ | $b_{\rm turb}$ | $\Delta b_{\rm turb}$ | $T[K]$ | $\Delta T[K]$ |
|---|---|---|---|---|---|---|---|---|---|---|
| CII | 12.241 | 0.054 | 3.5721363 | 0.0000006 | 5.2236 | //// | 2.27 | 1.16 | 16000 | 550 |
| CII | 12.799 | 0.019 | 3.5722686 | 0.0000004 | 6.7576 | //// | 4.62 | 0.38 | 17500 | 3980 |
| CII | 13.153 | 0.0076 | 3.5724579 | 0.0000004 | 7.7302 | //// | 5.71 | 0.11 | 19600 | 475 |
| SiII | 11.056 | 0.073 | 3.5721363 | 0.0000006 | 3.8243 | //// | 2.27 | 1.16 | 16000 | 550 |
| SiII | 11.913 | 0.012 | 3.5722686 | 0.0000004 | 5.6359 | //// | 4.62 | 0.38 | 17500 | 3980 |
| SiII | 12.2280 | 0.0059 | 3.5724579 | 0.0000004 | 6.6514 | //// | 5.71 | 0.11 | 19600 | 475 |
| FeIII | 10.7 | 8.8 | 3.5721363 | 0.0000006 | 3.1500 | //// | 2.27 | 1.16 | 16000 | 550 |
| FeIII | 12.740 | 0.070 | 3.5722686 | 0.0000004 | 5.1575 | //// | 4.62 | 0.38 | 17500 | 3980 |
| FeIII | 13.200 | 0.021 | 3.5724579 | 0.0000004 | 6.2031 | //// | 5.71 | 0.11 | 19600 | 475 |
| HI | 12.599 | 0.036 | 3.487132 | 0.000013 | 21.64 | 1.52 | //// | //// | ///// | //// |
| HI | 13.093 | 0.038 | 3.4874488 | 0.0000024 | 80.53 | 5.49 | //// | //// | ///// | //// |
| HI | 14.766 | 0.084 | 3.220962 | 0.000019 | 27.22 | 0.45 | //// | //// | ///// | //// |
| HI | 14.58 | 0.77 | 3.22113 | 0.00023 | 18.69 | 6.20 | //// | //// | ///// | //// |
| HI | 14.332 | 0.051 | 3.223848 | 0.000023 | 23.39 | 0.64 | //// | //// | ///// | //// |
| HI | 13.5147 | 0.0052 | 3.2256835 | 0.0000035 | 26.27 | 0.33 | //// | //// | ///// | //// |
| HI | 13.7353 | 0.0066 | 3.2195430 | 0.0000040 | 20.54 | 0.21 | //// | //// | ///// | //// |
| HI | 14.254 | 0.031 | 3.224541 | 0.000023 | 31.01 | 0.98 | //// | //// | ///// | //// |
| HI | 13.477 | 0.015 | 3.218005 | 0.000014 | 47.19 | 1.59 | //// | //// | ///// | //// |
| HI | 13.256 | 0.022 | 3.2192893 | 0.0000022 | 33.51 | 1.76 | //// | //// | ///// | //// |
| HI | 12.16 | 0.34 | 3.2178695 | 0.0000013 | 20.50 | 6.78 | //// | //// | ///// | //// |
| HI | 12.040 | 0.084 | 3.222880 | 0.000013 | 18.74 | 3.96 | //// | //// | ///// | //// |
| HI | 12.711 | 0.027 | 3.4818285 | 0.0000023 | 18.02 | 0.80 | //// | //// | ///// | //// |
| HI | 13.524 | 0.012 | 3.4826898 | 0.0000040 | 24.20 | 0.39 | //// | //// | ///// | //// |
| HI | 13.788 | 0.017 | 3.4833799 | 0.0000013 | 60.01 | 1.27 | //// | //// | ///// | //// |
| HI | 14.489 | 0.0071 | 3.4860540 | 0.0000012 | 26.58 | 0.20 | //// | //// | ///// | //// |
| HI | 12.545 | 0.050 | 3.4836095 | 0.0000016 | 12.13 | 1.12 | //// | //// | ///// | //// |
| HI | 13.204 | 0.061 | 3.484859 | 0.000012 | 62.40 | 7.25 | //// | //// | ///// | //// |
| HI | 12.368 | 0.071 | 3.4902918 | 0.0000008 | 29.06 | 3.84 | //// | //// | ///// | //// |
| HI | 11.8 | 1.6 | 3.4893665 | 0.0000028 | 15.53 | 12.1 | //// | //// | ///// | //// |
| HI | 11.8 | 1.6 | 3.4893778 | 0.0000027 | 20.96 | 15.9 | //// | //// | ///// | //// |
| HI* | 17.921 | 0.012 | 3.5721363 | 0.0000006 | 16.3941 | //// | 2.27 | 1.16 | 16000 | 550 |
| HI | 17.385 | ///// | 3.5722686 | 0.0000004 | 17.6299 | //// | 4.62 | 0.38 | 17500 | 3980 |
| HI | 17.471 | ///// | 3.5724579 | 0.0000004 | 18.8596 | //// | 5.71 | 0.11 | 19600 | 475 |
| DI* | 13.3490 | 0.0084 | 3.5721363 | 0.0000006 | 11.7479 | //// | 2.27 | 1.16 | 16000 | 550 |
| DI | 12.8097 | ///// | 3.5722686 | 0.0000004 | 12.9323 | //// | 4.62 | 0.38 | 17500 | 3980 |
| DI | 12.8956 | ///// | 3.5724579 | 0.0000004 | 13.9803 | //// | 5.71 | 0.11 | 19600 | 475 |
| HI | 13.998 | 0.003 | 3.5663711 | 0.0000020 | 26.48 | 0.22 | //// | //// | ///// | //// |
| HI | 13.651 | 0.005 | 3.5669595 | 0.0000013 | 38.93 | 0.41 | //// | //// | ///// | //// |
| HI | 13.004 | 0.014 | 3.5695045 | 0.0000014 | 30.56 | 0.86 | //// | //// | ///// | //// |
| HI | 14.239 | 0.020 | 3.564887 | 0.000016 | 36.01 | 1.41 | //// | //// | ///// | //// |
| HI | 13.4112 | 0.0059 | 3.5632944 | 0.0000041 | 31.67 | 0.40 | //// | //// | ///// | //// |
| HI | 12.94 | 0.16 | 3.5642678 | 0.0000017 | 20.72 | 1.60 | //// | //// | ///// | //// |
| HI | 11.59 | 0.11 | 3.567456 | 0.000013 | 4.72 | 1.51 | //// | //// | ///// | //// |
| HI | 13.191 | 0.086 | 3.5652367 | 0.0000099 | 11.10 | 0.73 | //// | //// | ///// | //// |
| HI | 11.66 | 0.13 | 3.5693771 | 0.0000073 | 6.55 | 1.88 | //// | //// | ///// | //// |
| HI | 12.106 | 0.058 | 3.568405 | 0.000029 | 21.75 | 3.11 | //// | //// | ///// | //// |
| HI | 13.586 | 0.096 | 3.564799 | 0.000018 | 13.87 | 1.72 | //// | //// | ///// | //// |
| HI | 14.514 | 0.014 | 3.5733392 | 0.0000018 | 24.35 | 0.20 | //// | //// | ///// | //// |
| HI | 12.788 | 0.026 | 3.5756356 | 0.0000016 | 30.01 | 1.45 | //// | //// | ///// | //// |
| HI | 12.065 | 0.086 | 3.574976 | 0.000019 | 15.75 | 2.33 | //// | //// | ///// | //// |

| | | | | | | | | | | |
|---|---|---|---|---|---|---|---|---|---|---|
| HI | 12.862 | 0.035 | 3.5746793 | 0.0000005 | 46.08 | 4.02 | //// | //// | ///// | //// |
| HI | 15.285 | 0.015 | 3.5730683 | 0.0000021 | 18.94 | 0.32 | //// | //// | ///// | //// |
| HI | 11.63 | 0.17 | 3.5699583 | 0.0000010 | 12.91 | 4.28 | //// | //// | ///// | //// |
| HI | 13.6515 | 0.0030 | 3.5766944 | 0.0000016 | 20.50 | 0.16 | //// | //// | ///// | //// |
| HI | 12.627 | 0.043 | 3.5772765 | 0.0000011 | 13.39 | 1.17 | //// | //// | ///// | //// |
| HI | 13.5442 | 0.0055 | 3.5777546 | 0.0000031 | 19.86 | 0.25 | //// | //// | ///// | //// |
| HI | 13.6344 | 0.0038 | 3.5784785 | 0.0000011 | 20.18 | 0.20 | //// | //// | ///// | //// |
| HI | 12.623 | 0.024 | 3.5801368 | 0.0000066 | 20.12 | 0.81 | //// | //// | ///// | //// |
| HI | 12.340 | 0.052 | 3.5795975 | 0.0000007 | 21.25 | 2.81 | //// | //// | ///// | //// |
| HI | 13.255 | 0.012 | 3.5817387 | 0.0000039 | 27.94 | 0.77 | //// | //// | ///// | //// |
| HI | 11.55 | 0.15 | 3.5810681 | 0.0000014 | 6.84 | 2.85 | //// | //// | ///// | //// |
| HI | 12.00 | 0.20 | 3.5817908 | 0.0000012 | 9.76 | 2.77 | //// | //// | ///// | //// |
| HI | 12.205 | 0.077 | 3.5789512 | 0.0000008 | 14.22 | 1.99 | //// | //// | ///// | //// |
| HI | 12.94 | 0.30 | 2.657051 | 0.000025 | 48.30 | 12.87 | //// | //// | ///// | //// |
| HI | 12.43 | 0.52 | 2.655951 | 0.000082 | 28.61 | 14.91 | //// | //// | ///// | //// |
| HI | 12.88 | 0.36 | 2.6606363 | 0.0000023 | 21.15 | 13.19 | //// | //// | ///// | //// |
| HI | 13.49 | 0.81 | 2.65930 | 0.00037 | 25.07 | 16.33 | //// | //// | ///// | //// |
| HI | 14.09 | 0.22 | 2.659670 | 0.000041 | 13.57 | 4.71 | //// | //// | ///// | //// |
| HI | 14.13 | 0.20 | 2.65990 | 0.00011 | 29.32 | 6.50 | //// | //// | ///// | //// |
| HI | 12.99 | 0.67 | 2.659302 | 0.000034 | 8.73 | 3.79 | //// | //// | ///// | //// |
| HI | 12.92 | 0.07 | 2.5698582 | 0.0000229 | 24.34 | 2.93 | //// | //// | ///// | //// |
| HI | 12.58 | 0.09 | 2.5710639 | 0.0000238 | 12.82 | 2.32 | //// | //// | ///// | //// |
| HI | 14.24 | 0.05 | 2.5738667 | 0.0000341 | 39.34 | 6.05 | //// | //// | ///// | //// |
| HI | 11.97 | 0.22 | 2.5748208 | 0.0000060 | 4.91 | 3.23 | //// | //// | ///// | //// |
| HI | 13.46 | 0.13 | 2.5745567 | 0.0000162 | 16.79 | 2.02 | //// | //// | ///// | //// |
| HI | 12.61 | 0.29 | 2.5730243 | 0.0000317 | 14.30 | 5.32 | //// | //// | ///// | //// |
| HI | 13.22 | 0.21 | 2.5754203 | 0.0000034 | 35.60 | 7.72 | //// | //// | ///// | //// |
| HI | 12.35 | 0.59 | 2.5257534 | 0.0000239 | 6.67 | 2.68 | //// | //// | ///// | //// |
| HI | 12.39 | 0.58 | 2.5258754 | 0.0001296 | 11.03 | 8.17 | //// | //// | ///// | //// |
| HI | 13.49 | 0.08 | 2.5256959 | 0.0000028 | 92.30 | 10.65 | //// | //// | ///// | //// |
| HI | 13.26 | 0.04 | 2.5278475 | 0.0000071 | 36.44 | 2.53 | //// | //// | ///// | //// |
| HI | 13.62 | 0.05 | 2.5296988 | 0.0000199 | 70.40 | 4.35 | //// | //// | ///// | //// |
| HI | 13.49 | 0.034 | 2.4992514 | 0.0000028 | 49.94 | 2.22 | //// | //// | ///// | //// |
| HI | 13.37 | 0.036 | 2.4994202 | 0.0000075 | 21.05 | 0.99 | //// | //// | ///// | //// |
| HI | 11.94 | 0.14 | 2.4829852 | 0.0000042 | 6.21 | 2.65 | //// | //// | ///// | //// |
| HI | 12.581 | 0.063 | 2.482227 | 0.000019 | 26.15 | 3.14 | //// | //// | ///// | //// |
| HI | 11.86 | 0.19 | 2.484349 | 0.000018 | 4.04 | 2.87 | //// | //// | ///// | //// |
| HI | 12.952 | 0.082 | 2.4867892 | 0.0000023 | 24.85 | 5.07 | //// | //// | ///// | //// |
| HI | 13.375 | 0.019 | 2.4863371 | 0.0000082 | 25.03 | 0.72 | //// | //// | ///// | //// |
| HI | 13.372 | 0.092 | 2.4711215 | 0.0000747 | 40.05 | 5.04 | //// | //// | ///// | //// |
| HI | 13.563 | 0.131 | 2.4715671 | 0.0000374 | 20.19 | 3.41 | //// | //// | ///// | //// |
| HI | 13.201 | 0.098 | 2.4727614 | 0.0000361 | 63.99 | 11.66 | //// | //// | ///// | //// |
| HI | 13.638 | 0.011 | 2.4753093 | 0.0000040 | 21.79 | 0.51 | //// | //// | ///// | //// |
| HI | 12.78 | 0.19 | 2.4729518 | 0.0000198 | 19.01 | 4.01 | //// | //// | ///// | //// |
| HI | 13.709 | 0.010 | 2.4748978 | 0.0000046 | 25.42 | 0.61 | //// | //// | ///// | //// |
| HI | 11.972 | 0.086 | 2.4740218 | 0.0000089 | 4.74 | 1.31 | //// | //// | ///// | //// |
| HI | 14.187 | 0.033 | 2.4632270 | 0.0000227 | 37.50 | 1.14 | //// | //// | ///// | //// |

Table A2: Interlopers that contribute as Lyman $\beta$ or Lyman $\gamma$ to the fitting regions. A limited number of transitions, marked as Unknown in the table, did not show a corresponding Lyman $\beta$ or $\gamma$ in the fitting regions but were required for convergence of the fit, and are thus listed here.

| Transition | Column density | $z$ | $b_{\rm tot}$ | Transition | Column density | $z$ | $b_{\rm tot}$ |
|---|---|---|---|---|---|---|---|
| HI | 13.725 | 3.33306 | 43.49 | HI | 11.916 | 3.18239 | 10.58 |
| HI | 14.148 | 3.33321 | 23.28 | HI | 13.646 | 3.14762 | 17.90 |
| HI | 12.940 | 3.33406 | 30.18 | HI | 13.024 | 3.14857 | 29.28 |
| Unknown | 12.598 | 3.33535 | 5.34 | HI | 12.610 | 3.14954 | 21.36 |
| Unknown | 12.597 | 3.33563 | 8.12 | HI | 13.833 | 3.15078 | 23.66 |
| Unknown | 11.553 | 3.33589 | 1.76 | HI | 13.421 | 3.15125 | 19.34 |

| | | | | | | | |
|---|---|---|---|---|---|---|---|
| HI | 13.411 | 3.33581 | 54.25 | HI | 13.606 | 3.37168 | 37.19 |
| Unknown | 12.272 | 3.33618 | 4.39 | HI | 13.817 | 3.37277 | 23.06 |
| Unknown | 11.898 | 3.33648 | 4.61 | HI | 13.606 | 3.37168 | 37.19 |
| HI | 12.929 | 3.33695 | 21.45 | HI | 13.817 | 3.37277 | 23.06 |
| HI | 13.057 | 3.33811 | 36.28 | HI | 13.079 | 3.37140 | 15.26 |
| HI | 13.096 | 3.33814 | 40.18 | HI | 12.646 | 3.37320 | 19.72 |
| HI | 14.352 | 3.23251 | 21.80 | HI | 12.692 | 3.37492 | 55.41 |
| HI | 13.885 | 3.23384 | 41.77 | HI | 12.299 | 3.37440 | 3.11 |
| HI | 15.119 | 3.23556 | 32.92 | HI | 12.732 | 3.37683 | 55.39 |
| HI | 13.058 | 3.23673 | 18.99 | HI | 11.766 | 3.37499 | 10.55 |
| HI | 14.528 | 3.23770 | 29.51 | HI | 11.977 | 3.37175 | 5.62 |
| HI | 13.482 | 3.23923 | 33.15 | HI | 11.729 | 3.37223 | 6.19 |
| HI | 14.000 | 3.23067 | 37.35 | HI | 12.366 | 3.12955 | 14.57 |
| HI | 14.305 | 3.45857 | 24.65 | HI | 15.049 | 3.13059 | 28.17 |
| HI | 13.724 | 3.44979 | 20.32 | HI | 13.106 | 3.13223 | 78.61 |
| HI | 14.512 | 3.45031 | 43.96 | HI | 13.229 | 3.35231 | 27.12 |
| HI | 14.421 | 3.45322 | 88.19 | HI | 12.866 | 3.35478 | 55.59 |
| HI | 12.919 | 3.45699 | 43.84 | HI | 12.777 | 3.35603 | 26.98 |
| HI | 14.519 | 3.45987 | 30.85 | HI | 12.410 | 3.35395 | 19.71 |
| HI | 15.161 | 3.46056 | 28.97 | HI | 12.602 | 3.35308 | 27.77 |
| HI | 14.495 | 3.46143 | 17.85 | HI | 11.914 | 3.35965 | 12.44 |
| HI | 14.067 | 3.46228 | 23.03 | HI | 11.645 | 3.35704 | 12.59 |
| HI | 14.682 | 3.46417 | 20.98 | HI | 13.759 | 3.11792 | 26.21 |
| HI | 13.028 | 3.46802 | 31.45 | HI | 13.026 | 3.11775 | 56.69 |
| HI | 12.746 | 3.46878 | 23.68 | HI | 12.681 | 3.12132 | 27.41 |
| HI | 13.187 | 3.46941 | 6.16 | HI | 12.512 | 3.11782 | 11.40 |
| HI | 13.391 | 3.46942 | 25.08 | HI | 12.566 | 3.11951 | 20.98 |
| HI | 13.907 | 3.46440 | 41.01 | HI | 12.133 | 3.12037 | 15.36 |
| HI | 12.853 | 3.45565 | 29.48 | HI | 12.933 | 3.11858 | 32.72 |
| HI | 14.793 | 3.45332 | 36.89 | HI | 12.711 | 3.11682 | 36.77 |
| HI | 13.088 | 3.46294 | 37.56 | HI | 12.087 | 3.11560 | 21.49 |
| HI | 12.318 | 3.46555 | 20.00 | HI | 12.919 | 3.09982 | 90.19 |
| HI | 11.745 | 3.45483 | 8.14 | HI | 13.998 | 3.10029 | 23.13 |
| HI | 13.224 | 3.45219 | 19.20 | HI | 12.387 | 3.10095 | 14.14 |
| HI | 13.684 | 3.17379 | 28.70 | HI | 12.624 | 3.10114 | 16.75 |
| HI | 13.983 | 3.17480 | 22.47 | HI | 13.323 | 3.10202 | 37.07 |
| HI | 14.200 | 3.17562 | 25.02 | HI | 13.491 | 3.10322 | 24.13 |
| HI | 13.688 | 3.17643 | 28.67 | HI | 12.267 | 3.10436 | 19.62 |
| HI | 13.295 | 3.17753 | 15.13 | HI | 12.370 | 3.10340 | 11.60 |
| HI | 14.373 | 3.17777 | 40.62 | HI | 11.603 | 3.10194 | 4.46 |
| HI | 13.669 | 3.17913 | 23.71 | HI | 12.971 | 3.10031 | 10.64 |
| HI | 13.726 | 3.18095 | 33.59 | HI | 12.213 | 3.10056 | 4.62 |
| HI | 13.075 | 3.18197 | 19.54 | HI | 12.981 | 3.32722 | 26.49 |
| HI | 13.458 | 3.18294 | 28.16 | HI | 13.716 | 3.32823 | 24.11 |
| HI | 12.910 | 3.18366 | 32.69 | HI | 13.051 | 3.33003 | 31.69 |
| HI | 13.479 | 3.18502 | 22.77 | HI | 13.107 | 3.33111 | 35.49 |
| HI | 12.429 | 3.17366 | 10.30 | HI | 13.143 | 3.32896 | 29.62 |
| HI | 12.178 | 3.18309 | 8.68 | HI | 13.082 | 3.32730 | 24.75 |
| HI | 12.991 | 3.17826 | 14.57 | | | | |

This paper has been typeset from a TEX/LATEX file prepared by the author.